

Using Microscopy and Magnetization Measurements to Characterize Electron Irradiation of Nb and Nb₃Sn

Calder Sheagren^{1,2} Tiziana Spina¹

1. Fermilab Applied Physics and Superconducting Technology
Division, Batavia IL 60510
2. The University of Chicago, Chicago IL 60637

Lee Teng Internship Final Report

Date: August 22, 2019

This manuscript has been authored by Fermi Research Alliance, LLC under Contract No. DE-AC02-07CH11359 with the U.S. Department of Energy, Office of Science, Office of High Energy Physics.

Abstract

Recently, high-energy irradiation experiments on industrial multifilamentary Nb₃Sn wires have been performed; previous work showed an enhancement in J_c with 24 GeV proton irradiation with fluences up to $\Phi t = 1.38 \times 10^{21} p/m^2$ [Spina, 2015] and an enhancement in J_c with 1 MeV neutron irradiation with fluences up to $\Phi t = 1 \times 10^{22} n/m^2$ [Baumgartner et al., 2013]. This enhancement is explained by an enhancement of the pinning force due to radiation-induced point pinning defects, in addition to the grain boundary pinning. However, this created a large amount of radioactivity, with $\tau_{1/2}$ on the order of magnitude of years. Thus, electron irradiation is a promising technique for creating artificial pinning centers, while minimizing the amount of radioactivity present. We present preliminary results for electron irradiation on Nb₃Sn wires and give upper bounds on effective fluences for J_c enhancement.

Furthermore, creating vacancies via electron irradiation is useful in the realm of SRF cavities, as vacancies can trap Hydrogen, preventing the formation of degradatory Nb-H compounds during cryogenic cooling. We present computer-aided microscopy analysis comparing hydride formation on Nb platelets before and after irradiation.

Contents

1	Introduction	3
2	Theoretical Framework	4
2.1	Lattice Description of Nb and Nb ₃ Sn	4
2.2	Hydride Growth on Nb Films	4
2.3	Flux Pinning	5
2.4	Analysis of Pinning Force Data	6
3	Computer Vision	8
3.1	Preliminaries	8
3.2	Edge Detection	10
3.3	Fourier Analysis Approach	11
3.4	Summary	12
4	Electron Irradiation and Nb-H Formation	12
4.1	Experimental Apparatus	13
4.2	Interactions between Radiation and Matter	14
4.3	Comparison of Gradient Mean Analysis and Filling Fraction Analysis	15
4.4	Critical Temperature Fitting	16
4.5	Warmup-Cooldown Comparisons	17
4.6	Irradiation Comparisons	17
4.7	Hydride Formation on Nb ₃ Sn Platelets	18
5	Electron Irradiation and Nb₃Sn Critical Parameters	19
5.1	Critical Temperature Considerations	19
5.2	Critical Current Density Considerations	21
5.3	Critical Field Considerations	23
6	Conclusion	23
A	Laplacian Formalism	25

1 Introduction

Nb and Nb₃Sn are materials used in large-scale accelerating structures: Nb and Nb₃Sn are used for superconducting radio frequency (SRF) cavities, and Nb₃Sn is used for superconducting magnets. It is useful to characterize the precipitate thermodynamics of Nb and the superconducting properties – critical temperature T_c , critical current density J_c , and upper critical field H_{c2} – of Nb₃Sn because of their impact on accelerator operation. We first discuss how the material properties of Nb impact its performance in cavities.

To have high-quality cavity resonators, surface resistance should be minimized, since

$$Q_0 = \frac{G}{R_s} = \frac{\omega\mu_0}{R_s} \cdot \frac{\int |\vec{H}|^2 dV}{\int |\vec{H}|^2 dA}, \quad (1)$$

and high- Q resonators have minimal power dissipation. We can write $R_s = R_{\text{res}} + R_{\text{BCS}} + R_B$, where R_{res} is a function of the conductance σ , R_{BCS} is a function of T/T_c , and R_B is the resistance accumulated by pinned magnetic fluxons, given by

$$R_B = \frac{b}{2} R_n, \quad (2)$$

where $b := B/B_{c2}$ is the reduced field, and B_{c2} is the upper critical field.

Flux pinning sites often occur at grain boundaries or other defects in the lattice like surface deformations caused by formation of Nb_{1-x}H_x, also denoted as Nb-H or niobium-hydride, compounds during cavity cool down. These hydrides are thought to be linked to the High-field Q slope (HFQS) phenomenon, and are usually mitigated by a 120°C mild bake [Charrier et al., 1998]. Investigating the behavior and mechanisms of hydride formation as a function of temperature is a necessary step to understand the fundamental properties of our material from a physical perspective.

Second, we discuss the importance of the superconducting parameters of Nb₃Sn as it relates to future accelerator operation. The critical temperature is important as it determines the operating the magnet: NbTi wires with $T_c \sim 10\text{K}$ cost more to operate than wires with Nb₃Sn wires with $T_c \sim 18\text{K}$.

The critical current density is important for fabricating magnets because we can increase the field of the operating magnet. For high-field magnets, we need $J_c \sim 10^9\text{A/m}^2$ at $B \sim 15\text{T}$; in the context of circular accelerators, stronger magnets help sustain a higher-energy beam.

It has been shown [Spina, 2015] that proton and neutron irradiation can be used to increase J_c in Nb₃Sn wires by creating artificial pinning centers, but this comes at a cost

of leaving the sample highly radioactive. Thus, electron irradiation becomes appealing as a potential mechanism for creating artificial pinning centers while reducing radioactivity, since it largely leaves the nuclear structure of the atoms intact. It is also thought [Spina et al., 2019, Barkov and Romanenko, 2012, Čížek et al., 2009] that irradiating cavity samples with electrons can create nucleation centers for hydride growth, and a large amount of nucleation centers implies fewer hydrides can grow due to the lower Hydrogen concentration. Before discussing the experimental setup and analysis techniques, we first explore the theory and motivation for the materials at hand.

2 Theoretical Framework

This section outlines the main theoretical framework describing the material properties of Nb and Nb₃Sn, particularly as they relate to RF cavities and superconducting magnets. In particular, we describe the mechanisms of hydride growth during cool down and the effects of electron irradiation on their formation.

2.1 Lattice Description of Nb and Nb₃Sn

In bulk metal, Nb forms a BCC crystal structure, which we can visualize by superimposing on a cube: Nb atoms occupy the vertices and center of the cube.

In agreement with the phase diagram [Charlesworth et al., 1970], Nb and Sn can combine to form Nb₃Sn, an intermetallic compound with an A15 structure. In an A15 lattice, Sn instead forms the BCC structure, with orthogonal Nb chains on the cubic faces. Counting atoms, there are 9 Sn atoms and 12 Nb atoms in one cube in the lattice.

2.2 Hydride Growth on Nb Films

In order for Nb-H precipitates to form on a Nb film, there needs to be a “starting point” for which the crystal to grow from; formally, this is called a *nucleation center* or *nucleation site*. These are thought to be results of Nb vacancies in the lattice, combined with 1,2, or 4 H atoms [Čížek et al., 2009]. This was confirmed by positron-annihilation spectroscopy, an imaging modality that is extremely sensitive to vacancies in metal.

Once the nucleation site forms, micron-scale or nanometer-scale structures can form, similar to those shown in Fig. 1, if there is a sufficient concentration of Hydrogen. Under-

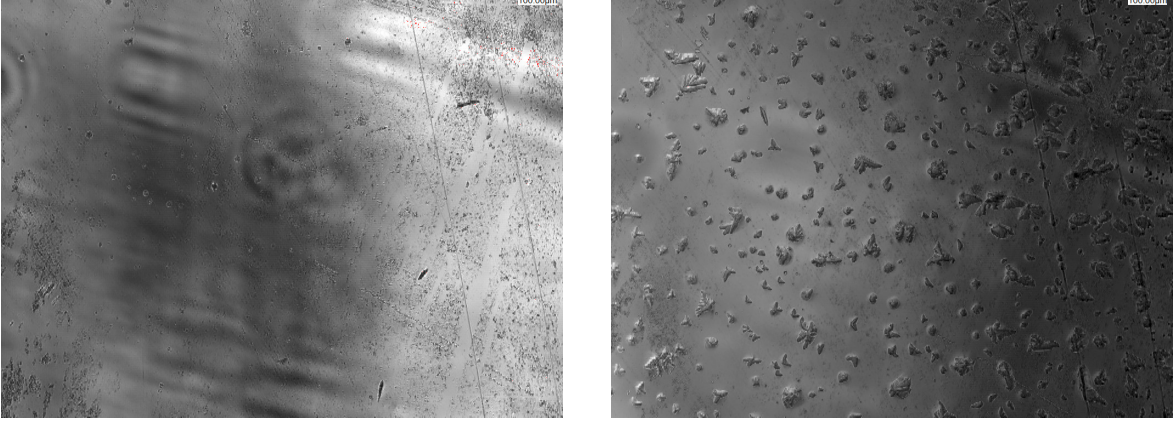


Figure 1: Nb samples as a function of temperature. (Left) Nb sample at $T = 272\text{K}$. (Right) Nb sample with hydride growth and surface deformation at $T = 80\text{K}$.

standing the growth of hydride structures as a function of temperature is a main focus of this paper.

2.3 Flux Pinning

When current flows through a superconductor, the superconductor feels a Lorentz force, with force density

$$\vec{F}_L = \vec{J} \times \vec{B}. \quad (3)$$

However, \vec{B} is quantized to integer multiples n of the *magnetic fluxon* $\Phi_0 = \frac{h}{2e} \approx 2.07 \times 10^{-15}\text{Vs}$, also called a *magnetic vortex*. The number n gives the number of flux lines per unit volume, and when $\vec{J} \ll \vec{J}_c$, the vortices are localized to their *pinning centers*, usually defects in the lattice with size close to the BCS coherence length ξ that trap magnetic field. This gives a *pinning force* F_p which describes the interaction between flux lines and pinning centers. Mathematically, this is

$$F_p = \eta L f_p, \quad (4)$$

where η is an efficiency factor, L is the length of the flux, and f_p is the linear pinning force density. Note that when $J = J_c$, balancing forces gives

$$\vec{F}_p = \vec{J}_c \times \vec{B}, \quad (5)$$

which is the quantity we measure.

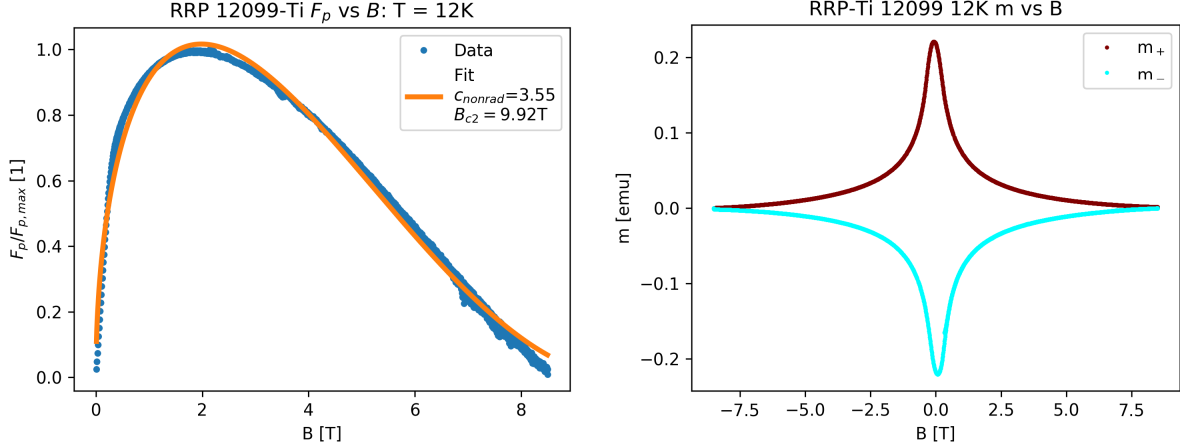


Figure 2: (Left) Fitted pinning force as a function of applied magnetic field. (Right) Magnetic moment as a function of applied field, with positive and negative moments noted. Negative values for the magnetic field correspond to a reversal of direction in the field.

The flux pinning force as a function of b has the scaling law

$$F_p(b) = Ab^p(1-b)^q, \quad (6)$$

where $A \in \mathbb{R}$, $p, q \in \mathbb{Q}$, and $b \in [0, 1]$. Additionally, \vec{F}_p is maximized when $b = \frac{p}{p+q}$. A sample fit of pinning force data as a function of external magnetic field is shown in Fig. 2.

There are two main types of pinning mechanisms we are interested in: grain boundary pinning ($p = 1/2, q = 2$), and point pinning ($p = 1, q = 2$). It is well known that before irradiation, flux pinning occurs due to grain boundary pinning, it was proved by other authors that proton and neutron irradiation creates artificial pinning centers, which increase the prevalence of point pinning effects [Spina, 2015, Baumgartner et al., 2013].

2.4 Analysis of Pinning Force Data

To calculate F_p , we need to first measure J_c ; in our apparatus, we measure J_c indirectly as a function of applied magnetic field. We probe the sample's magnetic moment as a result of the input field, and rapidly switch polarity, so we have a positive moment m_+ and a negative moment m_- . The full behavior of m vs B is shown in Fig. 2.

With m_+ and m_- measured, we can compute

$$J_c = \frac{3}{4} \cdot \frac{m_+ - m_-}{2NL(\rho_o^3 - \rho_i^3)}, \quad (7)$$

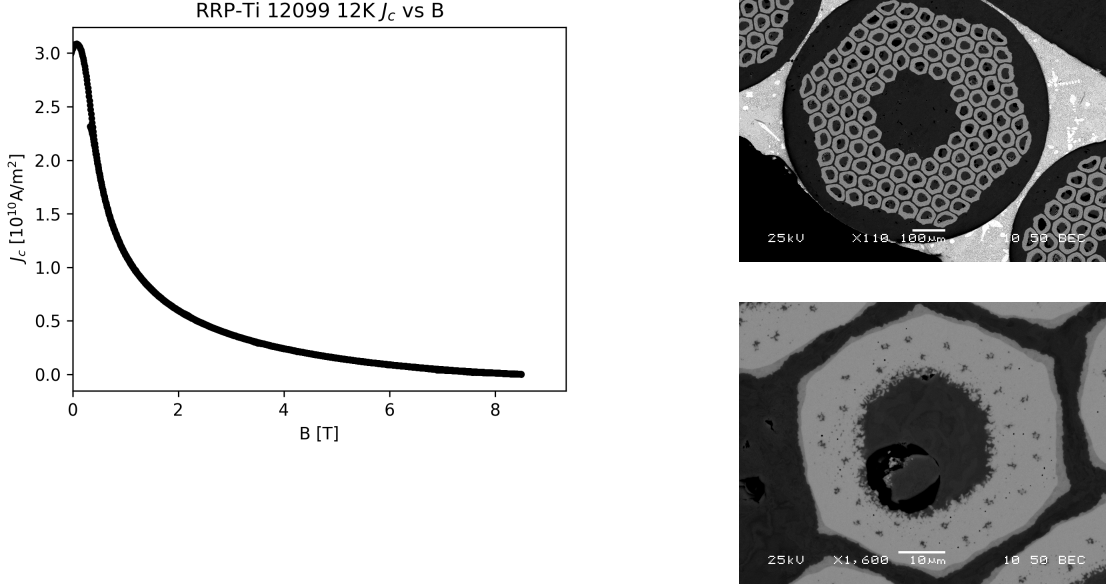


Figure 3: (Left) Critical current density as a function of applied magnetic field. (Right) SEM images of RRP12099-Ti Nb₃Sn wires. (Top Right) Cross-section of full RRP wire. (Bottom Right) Cross-section of single RRP element. (SEM Images courtesy of X. Xu)

where N is the number of subelements in the wire, L is the wire length, ρ_o is the outer radius of a subelement, and ρ_i is the inner radius of a element [Baumgartner et al., 2012]. We show J_c vs B behavior in Fig. 3.

When analyzing flux pinning data for wires, it is necessary to take into account the fabrication techniques and heat treatments used. RRP (Restack Rod Process) wires are produced starting from Nb, NbTa, or NbTi rods inserted into a Cu matrix, together with a central Sn core drawn to the final diameter. Long intermediate annealings are necessary to diffuse the Sn into the Cu matrix, to form Sn rich bronze, and to form the A15 phase. Very high A15 fractions, and thus high J_c overall values, can be obtained with this technique [Barzi et al., 2012]. PIT (Powder in Tube) Nb₃Sn wires are fabricated by filling Nb or NbTa tubes with NbSn₂, Sn, and Cu powders and subsequently inserting these tubes into a Cu matrix, cold-extruding them, and drawing them into the final diameter [Godeke, 2006]. In this paper, we only consider RRP wires.

The usual pinning force analysis for A15 structures only requires one term as described in Section 2.3, but after irradiation, a *two-mechanism model*, introduced by Spina and Baumgartner [Spina, 2015, Baumgartner et al., 2013], is necessary to fit the data for RRP Nb₃Sn wires to determine the type of flux pinning. The equation used to fit the data is shown

below:

$$F_p(b) = c_n b^{1/2} (1 - b)^2 + c_r b (1 - b)^2, \quad (8)$$

where c_n is the grain boundary coefficient, and c_r is the point pinning coefficient. B_{e2} and c_r are used as fitting parameters, while we fixed c_n at the value before irradiation. This assumes in our analysis that grain boundary pinning does not change after irradiation.

3 Computer Vision

A large fraction of this project relies on microscopy analysis of Nb samples, which we would like to quantify to more precision than our eyes can offer. One novel analysis technique for this work is *computer vision*, otherwise known as computational image analysis.¹ In this section, we use analogies with standard multivariable calculus to describe the operating principles of computer vision, as viewed from the framework of computer-aided diagnosis. No prior background in this area is assumed; for more information, see [Barrett et al., 2003].

3.1 Preliminaries

Recall that given a function $f \in C^2(\mathbb{R}^2, \mathbb{R})$, we can define the gradient magnitude as

$$|\nabla f| := \sqrt{\left(\frac{\partial f}{\partial x}\right)^2 + \left(\frac{\partial f}{\partial y}\right)^2} \quad (9)$$

and the Laplacian as

$$\Delta f := \frac{\partial^2 f}{\partial x^2} + \frac{\partial^2 f}{\partial y^2}. \quad (10)$$

The gradient magnitude gives an insight into how much the function changes as a function of position, and the Laplacian indicates the curvature of the function.

At its lowest level, a grayscale image is an m by n grid of numbers, where each pixel, denoted as (i, j) ,² has a number $x \in [0, 255]$ corresponding to the brightness of the image at that pixel location.³ Note that black pixels have numerical value 0, and white pixels

¹These principles operate in the background of image-processing programs such as ImageJ, however directly plotting image features as a function of temperature is novel in this context.

²By convention, the top left pixel is $(0, 0)$, with i and j values increasing as we move right and down respectively.

³Color images store three numbers at each pixel value corresponding to the Red, Green, and Blue intensity, respectively.

have numerical value 255. Given this formulation, we can view an image as a matrix $M \in [0, 255]^{m \times n}$.

However, we want to develop a discrete calculus for image manipulation, so a functional formation is required. A matrix $M \in [0, 255]^{m \times n}$ is equivalent to a function

$$f : [m] \times [n] \rightarrow [0, 255], \quad (11)$$

with a pixel (i, j) in an $m \times n$ lattice as an input, and a real number in $[0, 255]$ as an output. We often call such functions *image functions* or *digital functions*.

To describe spatial changes of image functions, we define the *difference operators*

$$\Delta_x f(i, j; h) := \frac{f(i+h, j) - f(i, j)}{h} \quad \Delta_y f(i, j; h) := \frac{f(i, j+h) - f(i, j)}{h} \quad (12)$$

that are the discrete analogues of partial derivatives. We usually choose $h = 1$ to investigate the behavior of neighboring pixels, so we can ignore the division by h . We then define the *discrete gradient magnitude* as

$$|\nabla f| = \sqrt{(\Delta_x f)^2 + (\Delta_y f)^2}, \quad (13)$$

which is an important tool for edge detection since larger gradient magnitudes correspond to larger differences in pixel grayscale value, which our eyes perceive as an edge. We define the *gradient mean* as the average value of the discrete gradient across the image.

Discretizing the Laplacian can be done in multiple ways, as described in Appendix A. In practice, however, it is not a good predictor of image behavior, but we include the formulae in the appendix for completeness.

The final image analysis tool described in this section is the notion of *convolution*, written in 2D continuous formalism as

$$(f * g)(x, y) := \int_{\mathbb{R}^2} f(a, b)g(x-a, y-b)da db. \quad (14)$$

Usually, f is the image function, and we denote g as the *convolution kernel*, written as a matrix $M \in M_2(\mathbb{Z})$ or $M_3(\mathbb{Z})$, that determines the type of transformation we apply to the image. We usually want $\sum_{i,j} M_{ij} = 0$ to avoid distorting the image. The convolution enjoys multiple nice properties, which are listed for 1D functions as Proposition 1.10 in [Sheagren, 2017].

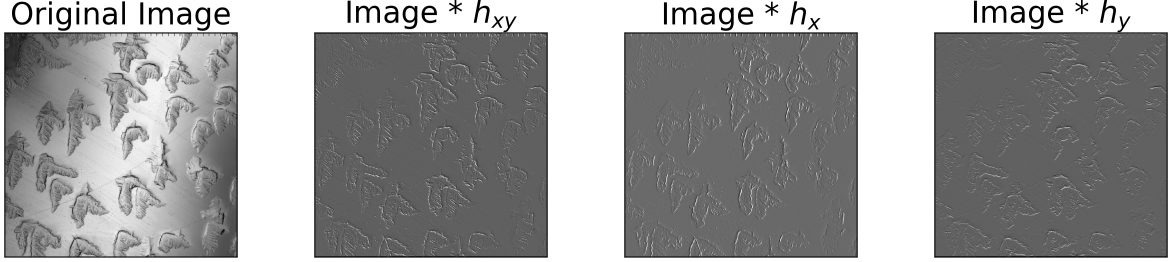


Figure 4: Comparison of convolution with Prewitt operators. (Left) Original Image. (Left Center) Image convolved with h_{xy} . (Right Center) Image convolved with h_x . (Right) Image convolved with h_y .

When discretizing a continuous function into an image function, the integral in Eq. 14 becomes a sum, meaning that we can write

$$(f * g)(i, j) = \sum_{a=1}^m \sum_{b=1}^n f(m, n)g(i - a, j - b). \quad (15)$$

Convolution is frequently used in image processing as a form of filtration, usually smoothing images or accentuating edges in them. In particular, the discrete gradient analysis here uses the *Sobel operator*, a convolution operator that detects image edges.

3.2 Edge Detection

Before performing gradient analysis, it is useful to “normalize” the images by accentuating edges, hence decorrelating the mean and gradient value. One particular way uses the *Prewitt operators*, the collection of which are shown below.

$$h_x = \begin{bmatrix} 1 & 0 & -1 \\ 1 & 0 & -1 \\ 1 & 0 & -1 \end{bmatrix}, \quad h_y = \begin{bmatrix} 1 & 1 & 1 \\ 0 & 0 & 0 \\ -1 & -1 & -1 \end{bmatrix}, \quad h_{xy} = \begin{bmatrix} 0 & 1 & 1 \\ -1 & 0 & 1 \\ -1 & -1 & 0 \end{bmatrix} \quad (16)$$

These detect horizontal, vertical, and diagonal edges respectively. Figure 4 shows the impact of convolving with Prewitt operators on Laser Confocal Microscope (LCM) images of Nb samples.⁴ This motivates the first step in the data processing sequence as convolving with h_{xy} to accentuate the relevant edges and reduce jitter in the sequence of images.

⁴Convolved images in Fig. 4 had contrast increased for improved visibility, but this increase in contrast appears nowhere in the process of data analysis.

3.3 Fourier Analysis Approach

In order to find the amount of surface deformations caused by hydrides as a fraction of the overall image, denoted as the *filling fraction*, a technique to distinguish the high spatial frequency areas from the low spatial frequency areas is needed. The goal of this technique is to count the pixels occupied by high-spatial frequency data, which we associate with edges in the image, heralding the presence of hydrides on the sample.⁵

A naive approach for counting edges would be to look throughout the image and count pixels that have large values of the discrete gradient. This is not optimal, however, since it is computationally tedious and does not accurately represent the increase of edges as temperature decreases. One alternate approach is to use region-growing algorithms, although these have not been implemented here due to the author's lack of experience with them. The process implemented in this analysis is based on Fourier analysis, and is described below in Algorithm 1 with visual examples of all steps in the process shown in Fig. 5. For this paper, let $f^\#$ denote the Fourier transform of f and f^\flat denote the inverse Fourier transform of f . Additionally, note that the expression $A \leftarrow B$ means that A is being set to the value B .

Algorithm 1 (Fourier Image Analysis).

Input: LCM image

Procedure:

(A) Fourier Transform the image: $\text{Image} \leftarrow \text{Image}^\#$

(B) Remove low-frequency data with cutoff frequency ν : $\text{Image} \leftarrow \text{Image} \cdot \begin{cases} 0, & \nu_x^2 + \nu_y^2 < \nu^2 \\ 1, & \text{else} \end{cases}$

(C) Inverse Fourier Transform filtered image: $\text{Image} \leftarrow \text{Image}^\flat$

(D) Binarize resulting image with cutoff grey value g : $\text{Image}_{i,j} \leftarrow \begin{cases} 1, & \text{Image}_{i,j} > g \\ 0, & \text{else} \end{cases}$.

(E) Filling Fraction = $\frac{1}{mn} \sum_{i=1}^m \sum_{j=1}^n \text{Image}_{i,j}$.

Output: Filling fraction of high-frequency data in image.

⁵Specifically, the filling fraction is defined as the percentage of high-frequency data in the image. This is useful for detecting hydride formation, but can be used as a tool in other contexts.

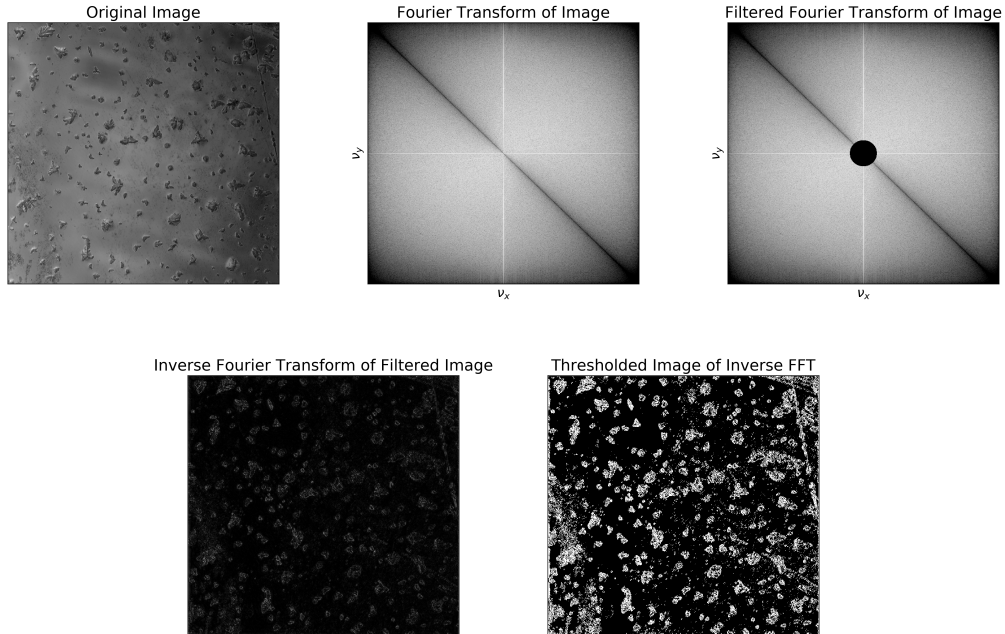


Figure 5: Visual representation of Algorithm 1. (Top Left) Original image. (Top Center) Step A. (Top Right) Step B. (Bottom Left) Step C. (Bottom Right) Step D.

This gives an efficient and powerful method for finding the amount of high-spatial frequency material in an overall image, with tunable parameters ν and g that can be customized as necessary for various applications. We use $\nu = 0.01, g = 25$ in this paper.

3.4 Summary

In summary, we view hydride formation on our sample as an increase edges on the image, which can be modeled as changes in the average discrete gradient magnitude of the images or an increase in areas with high spatial frequency in the images. To analyze this data, we track image features as a function of temperature to plot curves and fit those curves to extract parameters such as critical temperature and transition width.

4 Electron Irradiation and Nb-H Formation

To measure the effect of electron irradiation on hydride formation on Nb samples, we analyze LCM images of Nb cavity cutouts as a function of temperature, with $6\text{K} \leq T \leq 300\text{K}$. In

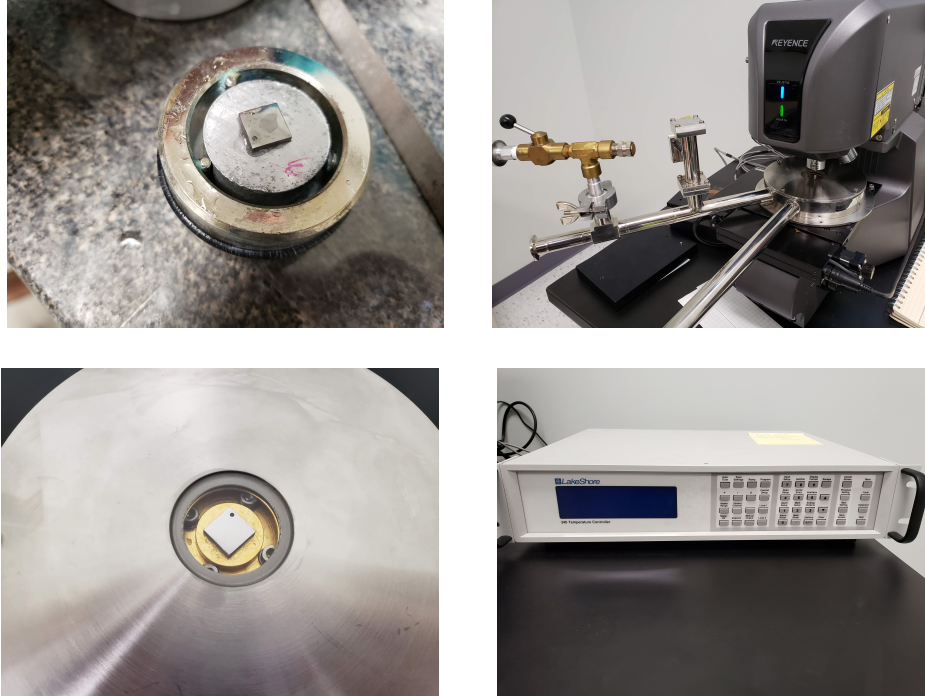


Figure 6: Hardware used for Nb-H cryo-microscopy experiment. (Top left) Mechanically polished cavity cutout sample. (Bottom left) Sample placed in cryogenic housing. (Top right) Laser Confocal Microscope with cryogenic housing inserted. (Bottom right) LakeShore temperature controller.

this section, we explain the hardware used to carry out this experiment, and the results we see.

4.1 Experimental Apparatus

We first H-load Nb cavity cutouts via a mechanical polish process: we use 300 grit sandpaper, 800 grit sandpaper, 1200 grit sandpaper, colloidal diamond solution, each for 15-20 minutes; finally, we place the sample in a vibratory polisher for 5-6 days with a $0.05\mu\text{m}$ colloidal silica solution.

Once the sample is polished, we place it in a cryogenic container, connected to a vacuum pump and a liquid He dewar. We then attach the cryogenic holder to the laser confocal microscope and take snapshots using the laser image while reading out the temperature using a LakeShore temperature controller. We also use the heater functionality of the temperature controller to accelerate the warm-up process.

A visual summary of this process is shown in Fig. 6. We now describe the physics behind the interactions of high-energy electrons with the metal lattice.

4.2 Interactions between Radiation and Matter

The main quantity of interest when bombarding matter with charged particles is the *stopping power*, or the energy loss dE per unit length dx . Symbolically, the Bethe-Block equation gives

$$S = -\frac{dE}{dx} = \frac{C_0 z^2 Z}{A\beta^2} \left[\ln \left(\frac{2mc^2(\gamma^2 - 1)}{I} \right) - \beta^2 \right] = S_n + S_e, \quad (17)$$

where $C_0 = 0.3071 \text{MeVcm}^2 \text{mol}^{-1}$ is a constant, z is the atomic number of the charged particle, Z and A are the atomic number and atomic mass of the medium being irradiated, $I \approx 9.1Z(1 + 1.9Z^{-2/3})$ is the mean excitation energy of the medium, and γ, β are the usual relativistic factor and relativistic velocity respectively [Podgoršak, 2010]. Here, we are most interested in the nuclear stopping power S_n , since that dictates the dynamics of electrons with Nb atoms in the lattice; electronic stopping power S_e is linked to radioactivity in the sample.

When a charged particle impinges on a Nb lattice, it may knock an atom out of place if it transfers kinetic energy T larger than the threshold energy E_d to the lattice atom. This lattice atom is called the *primary knock-on atom*, or PKA; in the case of Nb_3Sn , $E_d \approx 30 \text{eV}$. The displaced atom travels through the lattice encountering other lattice atoms, and if such encounters involve sufficient energy transfer ($T \geq E_d$), additional knockon atoms are created resulting in the production of a displacement cascade. The radiation damage event is concluded when the PKA comes to rest in the lattice as an interstitial atom. Lattice vacancies and interstitial atoms are known as *Frenkel pairs*; Frenkel pairs and clusters of Frenkel pairs in the lattice are the result of radiation damage [Spina, 2015].

When irradiating the Nb lattice, we increase the number of vacancies that are thought to be trapping centers for Hydrogen [Čížek et al., 2009]. This theoretically causes an increase in nucleation centers, meaning that fewer hydrides can form at each nucleation site [Spina et al., 2019].

When generalizing to multiple charged particles impinging on the lattice, it is useful to consider the *fluence* Φt , which tells us how many electrons impinged on the sample area; usual units are e^-/m^2 , p/m^2 , n/m^2 , etc.

We will consider data arising from two cavity cutouts in this paper: a non-irradiated sample # 5A and an irradiated sample # 2A ($\Phi t = 1.18 \times 10^{21} e^-/\text{m}^2$). Note that while the

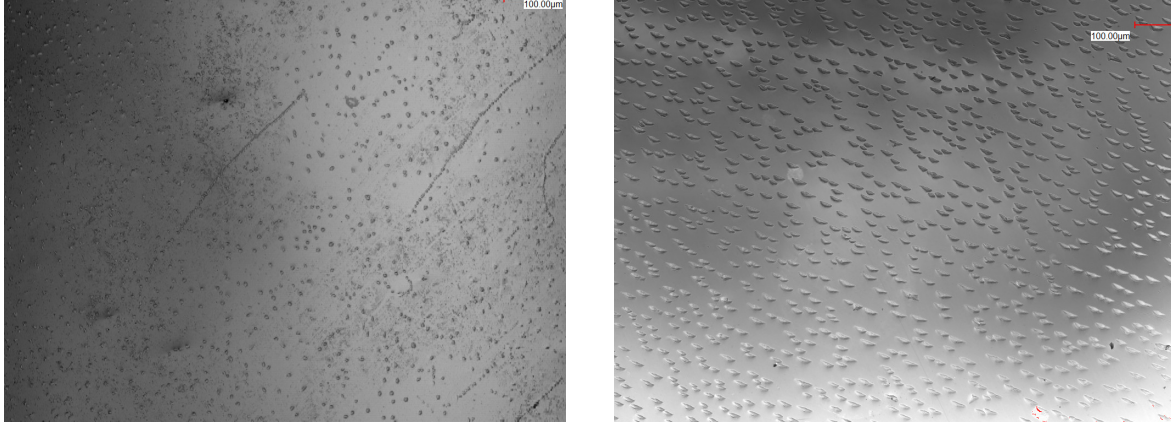


Figure 7: Profile of hydrides for Nb cavity cutout samples. (Left) # 5A (Non-irradiated). (Right) # 2A (Irradiated).

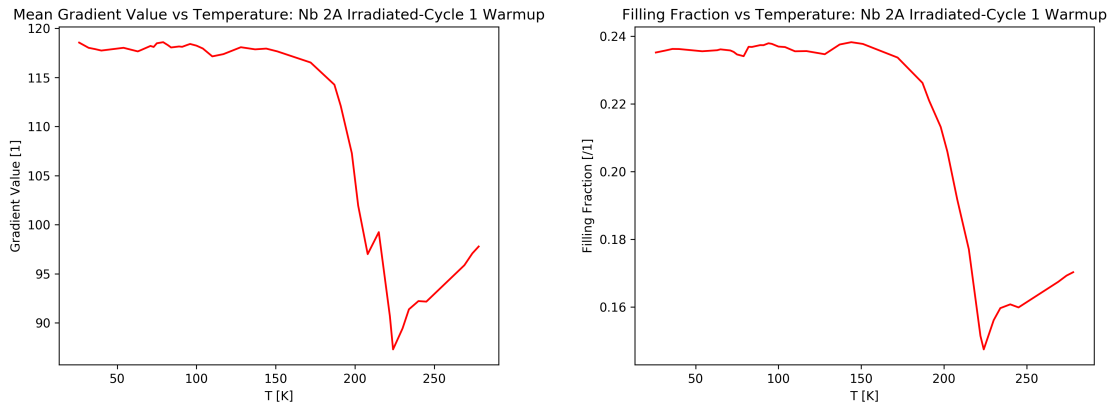


Figure 8: Comparison of analysis techniques for microscopy samples. (Left) Gradient Mean. (Right) Filling Fraction.

mechanical polishing process is identical for both samples, they are not necessarily from the same cavity, and are not assumed to have the same pre-processing before the mechanical polish. This may affect the profile of the hydrides and require more investigation in the future; the profile of hydrides for samples # 2A and # 5A is shown in Fig. 7.

4.3 Comparison of Gradient Mean Analysis and Filling Fraction Analysis

As described in Section 3, there were two main methods of analyzing microscopy images: mean discrete gradient and filling fraction; see Fig. 8 for a visual comparison. Comparing the

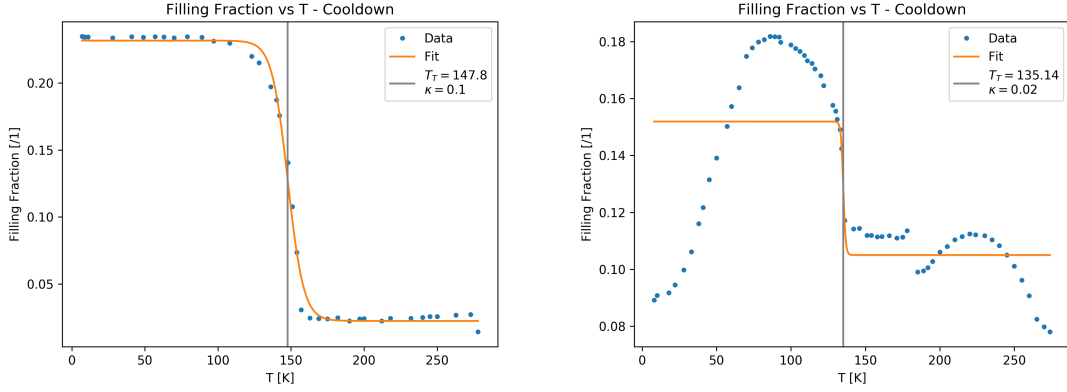


Figure 9: Sample fits of filling fraction plots for irradiated samples (Left) and non-irradiated samples (Right).

two, we see largely the same behavior between the two methods, although the gradient mean is more sensitive to sudden changes in exposure of the image; in this context, sudden changes in exposure result in sharp changes in the data, and resilience to changes in low-frequency image data is desired. Furthermore, the filling fraction has more physical significance than the gradient mean, so we only consider filling fraction analysis in the sections to come.

4.4 Critical Temperature Fitting

Given a plot of filling fraction as a function of temperature, it is useful to derive a threshold temperature T_T for hydride formation, so a method for fitting the data is required. Making an analogy with DC resistivity vs temperature data, (see Fig. 3 in [Sheagren et al., 2019]) we fit to the functional form

$$\text{F.F.}(T) = A \arctan(\kappa(T_T - T)) + B, \quad (18)$$

so that there is a smooth transition from $\text{F.F.} = B - A/2$ to $\text{F.F.} = B + A/2$ at $T = T_T$. Here, κ is a parameter that lends insight to the transition width, or the rate at which hydrides form as a function of temperature. While this fitting mechanism works well for irradiated samples, a different functional form is needed for non-irradiated samples, although it can be used to give a crude approximation of the hydride critical temperature. Sample fits can be shown in Fig. 9.

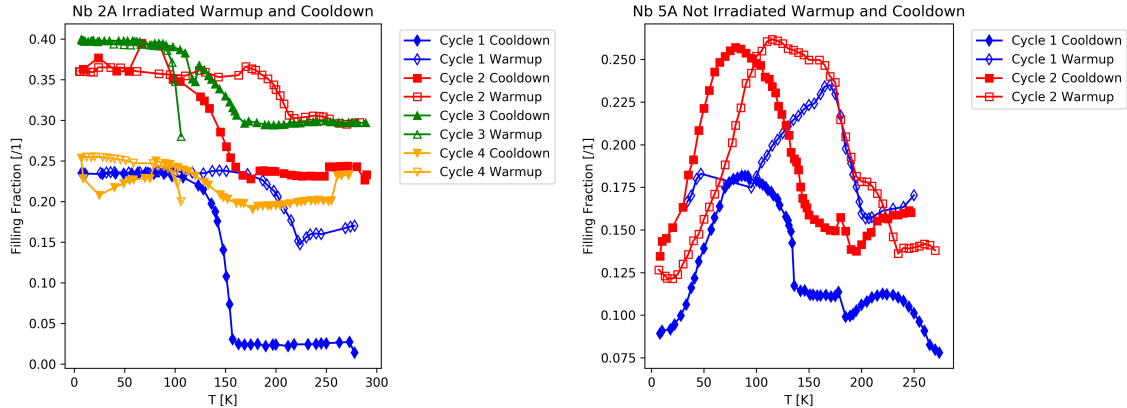


Figure 10: Comparison of warmup data with cooldown data for an irradiated sample (Left) and a non-irradiated sample (Right). Note that cycle 3 warmup and cycle 4 warmup for sample # 2A had a large amount of condensation due to a lack of vacuum pressure, so data points from images exclusively showing condensation phenomena were excluded. Additionally, only two cycles were conducted on sample # 5A due to time constraints and the hydride profile present – the small size implies that future cycles will closely mimic the cycle 2 behavior.

4.5 Warmup-Cooldown Comparisons

The behavior of hydrides on Nb samples is highly dependent on whether the sample is warming up or cooling down due to the dynamics of hydrogen in the metal and activation energies of the formations $\text{Nb} + \text{H} \rightarrow \text{Nb-H}$. Furthermore, the rate of temperature change (nominally 6K/minute) and time to capture and save the snapshot introduces an uncertainty in temperature of about $\sigma_T = 1\text{K}$.

When comparing warmup vs cooldown behavior in Fig. 10, we see that after the first cooldown, the filling fraction is never able to return to its original value, confirming that the damage done to the sample is irreversible. Additionally, we see that the critical temperature for hydride formation on cooldown is lower than the critical temperature for hydride disappearance on warmup, which has been observed previously [Spina et al., 2019].

4.6 Irradiation Comparisons

Comparing samples before and after irradiation is difficult, since the pre-processing and polishing is not identical between samples. Furthermore, it is impossible to test a sample, irradiate it, and retest it successfully since hydride growth has irreparably damaged the sample. Cutting a sample in half after polishing and irradiating half of it is a possible

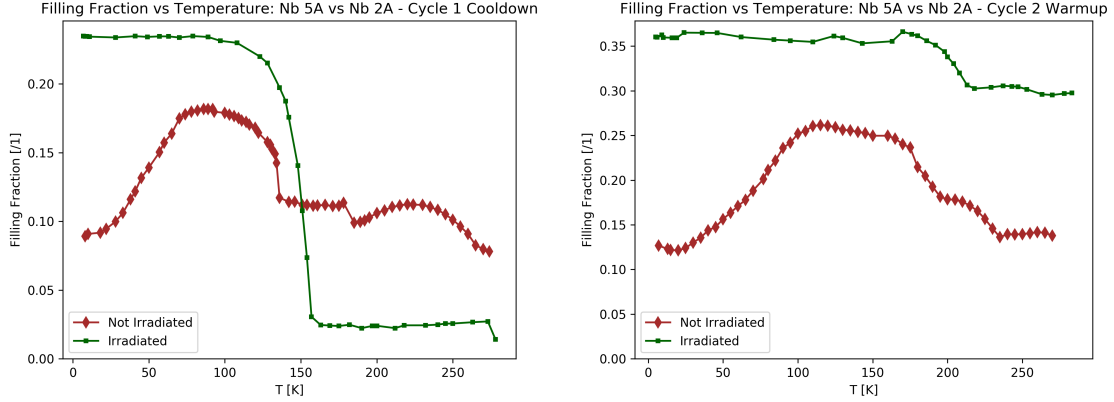


Figure 11: Comparison of data from irradiated samples and non-irradiated samples for cooldown (Left) and warmup (Right).

method, but the surface is likely to get scratched from the saw blade. Here, we compare different samples in Fig. 11 and come to conclusions that should be verified with more data.

The first takeaway from these comparisons is that the profile of the data is completely different between the irradiated samples and the non-irradiated samples: the irradiated samples have a well-defined transition, whereas the non-irradiated samples have a well-defined peak with a “bell-like” shape. The decrease in filling fraction for non-irradiated samples is speculated to be due to hydride growth which causes image smoothness to increase and filling fraction to decrease. In contrast, the vacancies created on irradiated samples prevent this large growth, so the filling fraction is relatively constant below the critical temperature.

The second takeaway is that the threshold temperatures and hydride phases are different. On cooldown, the irradiated samples have a higher threshold temperature, and on warmup, the irradiated samples have a single threshold temperature, whereas the non-irradiated samples have two transitions that correspond to different hydride phases on the sample.

The third takeaway is that there are more edges in the irradiated samples, corresponding to an increase in sharp surface deformations that herald the presence of nucleation centers.

4.7 Hydride Formation on Nb_3Sn Platelets

We repeated the cryo-microscopy experiment on non-irradiated H-loaded Nb_3Sn platelets, prepared with the Hot Isostatic Pressure technique [Spina, 2015], to obtain information on their behavior as a function of temperature. There was no observable visual difference

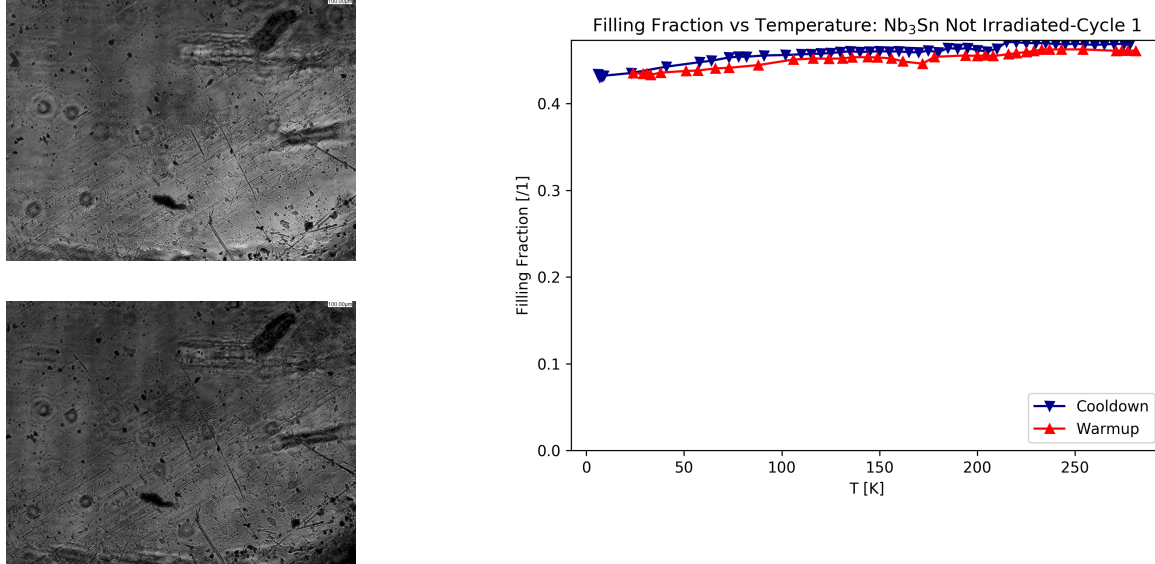


Figure 12: (Left) LCM images of Nb₃Sn at various temperatures: (Top) $T = 278\text{K}$. (Bottom) $T = 6\text{K}$. (Right) Filling Fraction plot for Nb₃Sn cooldown and warmup.

between the samples at room temperature and $T = 6\text{K}$, as shown in Fig. 12, alongside the Filling Fraction plot. No visible hydride formation was observed, so these samples were not irradiated; no further comparison is needed.

5 Electron Irradiation and Nb₃Sn Critical Parameters

5.1 Critical Temperature Considerations

We measure the critical temperature of Nb₃Sn wires using a Vibrating Sample Magnetometer (VSM) attached to a Quantum Design Physical Properties Measurement System (PPMS). Specifically, the magnetic moment decreases as the critical temperature threshold is crossed; we define the critical temperature as the onset temperature where the magnetic moment begins to sharply decrease; we additionally normalize the magnetic moment by sample length to account for volumetric differences in the wires⁶. A sample plot is shown in Fig. 13.

Furthermore, external magnetic fields affect the behavior of the sample upon cooldown; we subdivide this into two cases. First, when $B \ll 1\text{T}$, there is *zero field cooling* (ZFC), and the magnetic field is fully expelled by the sample. However, when B is no longer negligible, there is *field cooling* (FC) arising from trapped flux in the wire [Sandim et al., 2012]. When

⁶Formally, we assume that the cross-sectional area is unchanging with position z along the wire

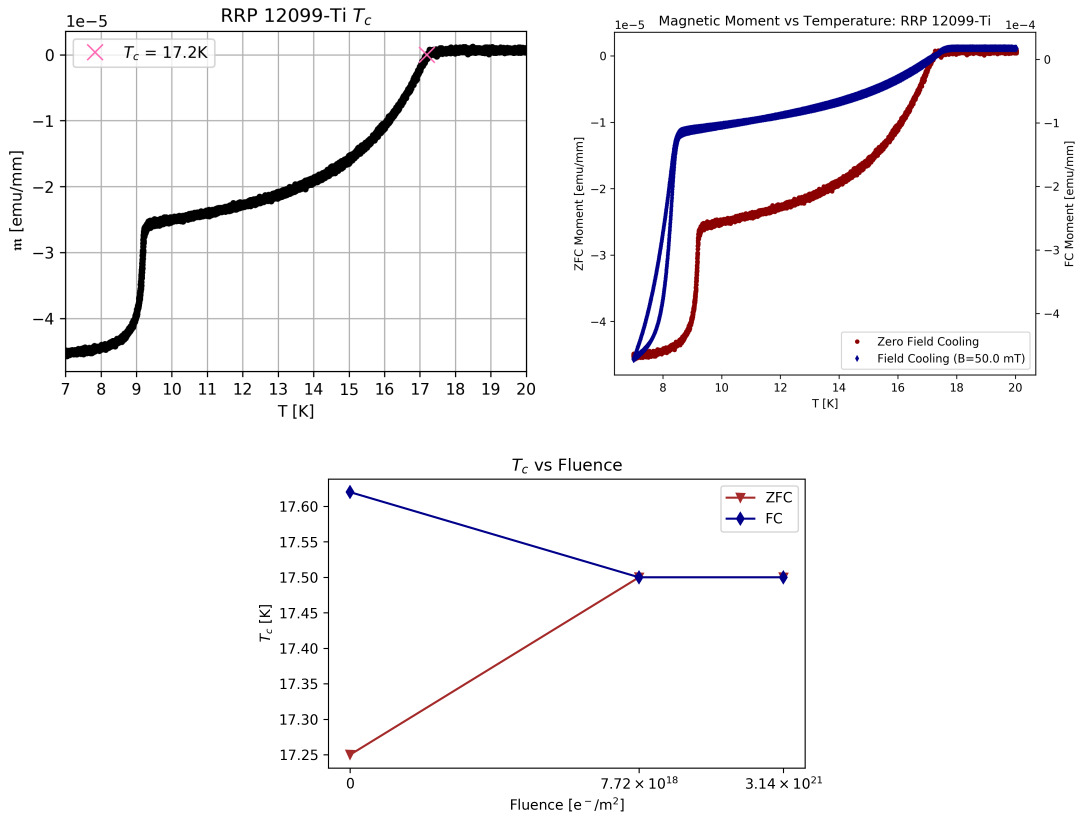


Figure 13: (Top Left) Sample T_c plot, with onset critical temperature labeled. (Top Right) Comparison of field cooled T_c vs zero field cooled T_c . (Bottom) Comparison of onset T_c as a function of fluence.

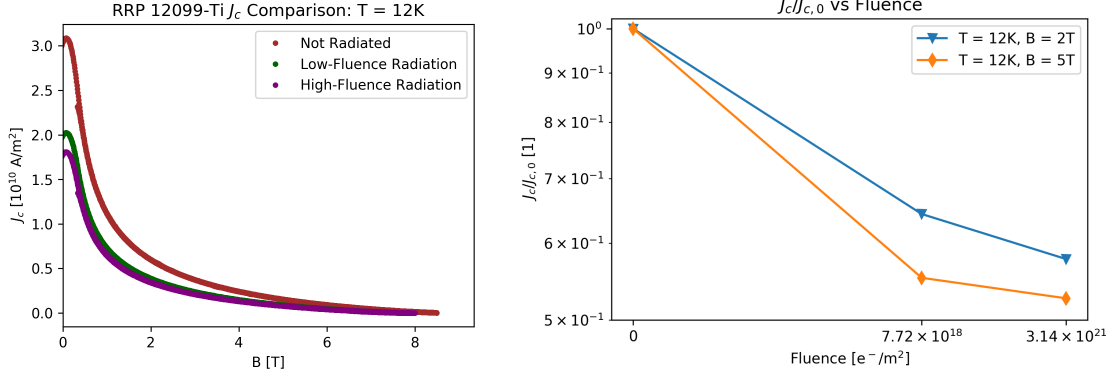


Figure 14: (Left) J_c vs B plots for each fluence. (Right) Comparison of J_c values as a function of fluence.

testing field-cooled behavior, we use a magnetic field of $B = 50$ mT. The behavior of field cooled vs zero field cooled measurements is shown in Fig. 13, alongside the change in T_c with fluence.

5.2 Critical Current Density Considerations

Fig. 2 shows the critical current density profile for the RRP wire as a function of applied magnetic field. When irradiating the sample, we expect to create artificial pinning centers that increase the critical current density.

This was not seen in the data, however, as the critical current density decreased monotonically with fluence; a 35% - 42% decrease was observed at a moderate fluence of $7.72 \times 10^{18} e^-/m^2$, and a 44%-47% decrease was observed at a high fluence of $3.14 \times 10^{21} e^-/m^2$. Plots of J_c vs fluence are shown in Fig. 14.

Furthermore, when analyzing the pinning force for irradiated samples, the two-mechanism approach does not accurately fit the data, whereas the data agrees largely with predictions given a non-irradiated model that only takes into account grain boundary pinning, see Fig. 15. This motivates the interpretation that electron irradiation with the stated fluences does not create artificial pinning centers as in the proton case [Spina, 2015]. We can thus conclude that only fluences $\Phi t < 7 \times 10^{18} e^-/m^2$ have the possibility of creating artificial pinning centers in RRP Nb₃Sn wire, although more work on lower-fluence irradiation is needed.

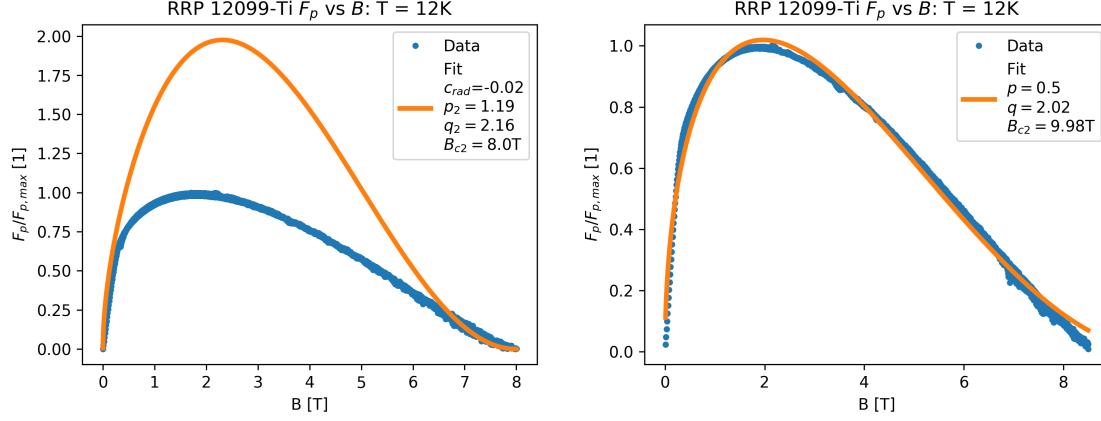


Figure 15: Comparison of fitted F_p vs B plots for a highly irradiated sample. (Left) Fitting done using two-mechanism approach. (Right) Fitting done using exclusively grain-boundary pinning mechanism.

	$\Phi t = 0e^-/m^2$	$\Phi t = 7.72E18e^-/m^2$	$\Phi t = 3.14E21e^-/m^2$
$T = 12K$	9.96T	9.98T	9.98T
$T = 13K$	7.88T	7.93T	7.93 T
$T = 14K$	5.72T	5.75T	5.57T
$T = 15K$	3.82T	3.85T	3.85T
$T = 16K$	2.02T	2.00T	2.00T
$T = 17K$	0.44T	0.44T	0.44T

Table 1: B_{c2} values for RRP12099-Ti wire as a function of temperature and fluence.

5.3 Critical Field Considerations

We use the result of the pinning force fit to estimate the critical field of the wires as a function of temperature and fluence. We see minimal variation in the critical field as a function of irradiation at each stage temperature. In particular, the two irradiated samples are nearly identical, mirroring the critical temperature behavior; these results are shown in Table 1.

6 Conclusion

In conclusion, Nb and Nb₃Sn samples were irradiated and tested using microscopy and magnetization measurements. Computer vision analysis on the microscopy data showed differences in profile, threshold temperature, and hydride phases when irradiating Nb platelets, and confirmed the lack of hydride growth in Nb₃Sn. Magnetization measurements showed a degradation of J_c and pinning force in Nb₃Sn wires with irradiation, although irradiation with lower fluences will be carried out.

Acknowledgements

CS would like to thank his mentor Tiziana Spina and his supervisor Peter Garbincius for their help throughout the program. CS would also like to thank Zuhawn Sung and Rob Schuessler for helping with laboratory equipment, Xingchen Xu for providing the RRP wires and SEM images, and finally Alex Romanenko and the SRF division for being welcoming and supportive.

This manuscript has been authored by Fermi Research Alliance, LLC under Contract No. DE-AC02-07CH11359 with the U.S. Department of Energy, Office of Science, Office of High Energy Physics.

References

- [Barkov and Romanenko, 2012] Barkov, F. and Romanenko, A. (2012). Direct Observation of Hydrides Formation in Cavity-Grade Niobium. *Phys. Rev. ST Accel. Beams*, 15:122001.
- [Barrett et al., 2003] Barrett, H. H., Myers, K. J., and Dhurjaty, S. (2003). Foundations of image science. *J. Electronic Imaging*, 14:029901.
- [Barzi et al., 2012] Barzi, E., Bossert, M., Gallo, G., Lombardo, V., Turrioni, D., Yamada, R., and Zlobin, A. (2012). Studies of Nb₃Sn strands based on the restacked-rod process for high-field accelerator magnets. *IEEE Transactions on Applied Superconductivity*, 22.
- [Baumgartner et al., 2013] Baumgartner, T., Eisterer, M., Weber, H. W., Flükiger, R., Scheuerlein, C., and Bottura, L. (2013). Effects of neutron irradiation on pinning force scaling in state-of-the-art Nb₃Sn wires.
- [Baumgartner et al., 2012] Baumgartner, T., Eisterer, M., Weber, H. W., Flükiger, R., Bordini, B., Bottura, L., and Scheuerlein, C. (2012). Evaluation of the critical current density of multifilamentary nb₃sn wires from magnetization measurements. *IEEE Transactions on Applied Superconductivity*, 22(3):6000604–6000604.
- [Charlesworth et al., 1970] Charlesworth, J. P., Macphail, I., and Madsen, P. E. (1970). Experimental work on the niobium-tin constitution diagram and related studies. *Journal of Materials Science*, 5(7):580–603.
- [Charrier et al., 1998] Charrier, J. P., Coadou, B., and Visentin, B. (1998). Improvements of superconducting cavity performances at high accelerating gradients. In *Proceedings of the 6th European Particle Accelerator Conference*, pages 1885–1887.
- [Godeke, 2006] Godeke, A. (2006). Topical review: A review of the properties of Nb₃Sn and their variation with A15 composition, morphology and strain state. *Superconductor Science & Technology - Supercond. Sci. Technol.*, 19.
- [Čížek et al., 2009] Čížek, J., Procházka, I., Daniš, S., Brauer, G., Anwand, W., Gemma, R., Nikitin, E., Kirchheim, R., Pundt, A., and Islamgaliev, R. K. (2009). Hydrogen-vacancy complexes in electron-irradiated niobium. *Phys. Rev. B*, 79:054108.
- [Podgoršak, 2010] Podgoršak, E. B. (2010). *Radiation Physics for Medical Physicists*. Springer-Verlag Berlin Heidelberg, second edition.

[Sandim et al., 2012] Sandim, M., Stamopoulos, D., Aristomenopoulou, E., Zaefferer, S., Raabe, D., Awaji, S., and Watanabe, K. (2012). Grain structure and irreversibility line of a bronze route CuNb reinforced Nb₃Sn multifilamentary wire. *Physics Procedia*, 36:1504 – 1509. Superconductivity Centennial Conference 2011.

[Sheagren, 2017] Sheagren, C. (2017). Uncertainty principles with fourier analysis.

[Sheagren et al., 2019] Sheagren, C., Anferov, A., Barry, P., Schuster, D., Shirokoff, E., and Tang, Q. Y. (2019). Atomic layer deposition niobium nitride films for high-Q resonators.

[Spina, 2015] Spina, T. (2015). *Proton irradiation effects on Nb₃Sn wires and thin platelets in view of High Luminosity LHC upgrade*. PhD thesis, CERN.

[Spina et al., 2019] Spina, T., Grassellino, A., Geelhoed, M., and Romanenko, A. (2019). Electron irradiation effects on hydrides formation in Nb for srf cavity. SRF 19 Dresden.

A Laplacian Formalism

We can describe the Laplacian formalism in two ways. First, we can view it as a second difference equation, similar to the discrete gradient.

$$\begin{aligned} \Delta f(i, j) &= \frac{\Delta_x f(; h) + \Delta_y f(; h)}{h} - \frac{\Delta_x f(; -h) + \Delta_y f(; -h)}{h} \\ &= \frac{f(i - h, j) + f(i + h, j) + f(i, j - h) + f(i, j + h) - 4f(i, j)}{h^2}. \end{aligned} \quad (19)$$

We can also view the Laplacian as a convolution operator, using the kernel

$$\mathbf{D} = \begin{bmatrix} 0 & 1 & 0 \\ 1 & -4 & 1 \\ 0 & 1 & 0 \end{bmatrix} \quad (20)$$

as an approximation for the second derivative.